

Quantitative Depth Profiling of Biporous Nickel Electrodes by Frequency-Domain Laser-Induced Photoacoustic Spectroscopy

ANDREAS MANDELIS* and JOHN D. LYMER

Photoacoustics Laboratory, Department of Mechanical Engineering, University of Toronto, 5 King's College Road, Toronto, Ontario M5S 1A4, Canada

Frequency-domain Photoacoustic Spectroscopy (PAS) was used with a He-Ne laser exciting beam to probe commercially available, powdered and pressed nickel electrodes with dual-porosity profiles. The frequency response of the electrodes was shown to be capable of providing quantitative information about the thermal conductivity and diffusivity of each of the two porous layers, provided the depth of the porosity junction in the electrode bulk is known. The reasonable agreement of the experimental data with a one-dimensional mathematical model of the photoacoustic response from a two-layer, photoacoustically saturated, continuous system indicates that powdered and pressed nickel electrodes behave photoacoustically approximately like a simple continuous composite-layer solid. This conclusion, together with experimental PAS results from uniporous electrodes, emphasizes the high potential of photoacoustic spectroscopy as a nondestructive, depth profiling, analytical technique for the determination of complex porosity profiles in electrodes manufactured for use in electrochemical energy conversion devices, such as fuel cells.

Index Headings: Laser-induced photoacoustic spectroscopy; Variable electrode porosities; Frequency response; Quantitative analysis; Fuel cells.

INTRODUCTION

Porous nickel electrodes are conventionally used in hydrogen-oxygen fuel cells in the presence of either acidic or basic electrolytes. Such electrodes provide large numbers of adsorption sites suitable for the chemical reaction between the electrolyte and the gases. They also provide low resistivity paths for the flow of electrons to and from the reaction sites.^{1,2} An important technological requirement for the long-term stability and high efficiency of electrochemical energy conversion in fuel cells is the ability of the electrodes to act as interfaces between the electrolyte and the gases so that the former does not leak into the gas chambers and the latter do not penetrate into the electrolyte. This requirement can be met, in principle, by the use of biporous nickel electrodes.¹ The combination of a fine-pore and a coarse-pore layer in the electrode prevents the electrolyte from leaking into the gas chamber by virtue of a small pressure differential of the fine-pore/coarse-pore interface: when the electrolyte is in contact with the fine-pore layer, the capillary forces which draw it into the electrode bulk are sharply reduced at the boundary of the coarse-pore layer.¹ This effect, in turn, tends to keep the electrolyte at the fine-pore/coarse-pore interface even for gas pressures slightly higher than that of the electrolyte, which thus prevents the gas/electrolyte interface from moving further into the electrode toward the electrolyte

chamber. It is therefore important to have an accurate knowledge of the possible degradation mechanism(s) of the two layers of different porosity in nickel electrodes due to the wetting action and penetration of the electrolyte as well as to be able to measure nondestructively the degree of porosity homogeneity throughout a given layer. The latter requirement is of paramount importance to the controllability of the electron transfer process(es) within the bulk of the electrode, so good reliability of the fuel cell performance curves (Tafel plots) can be ascertained. Presently available methods for acquiring porosity-gradient and layer-homogeneity information from nickel electrodes are destructive, as they require cutting of the electrode and further processing which enhances the visibility of the porous regions under an optical microscope or an image analyzer.

In this paper we report the first nondestructive application of Laser-Induced Photoacoustic Spectroscopy to the determination of the thermal parameters, conductivity and diffusivity, in commercially available, nominally dual-porosity nickel electrodes, in which the thicknesses of both porous layers were known. The experimental results and the subsequent analysis based on a one-dimensional model show that PAS can be successfully used as a fast, nondestructive, sensitive quantitative probe of these materials' thermal properties. It is therefore suitable for fuel cell electrode degradation process monitoring *in situ*, since such processes tend to alter locally the values of the bulk electrode thermal parameters, as a result of the penetration of the porous material by the gas or the liquid phase.

EXPERIMENTAL

The photoacoustic apparatus used in the present work is shown in Fig. 1a. A 5-mW He-Ne laser beam was mechanically modulated with an AMKO OC 4000 chopper (Wissenschaftlich-Technische Instrumente GmbH) between 10 Hz and 2 kHz. The PAS signals from an EG&G Model 6003 photoacoustic cell were monitored with the use of an EG&G 5204 lock-in analyzer. A fused silica beam splitter was also available for spectra acquisition (Fig. 1b) for directing ~7% of the laser light to a fast pyroelectric detector (ORIEL Model 7090-2), whose output was connected to an EG&G 5204 lock-in analyzer with a ratio option for normalized PAS spectra acquisition. The beam splitter was only inserted in the optical path when UV-VIS range photoacoustic spectral information from the electrodes was required, as shown in Fig. 1b, with a 1000 W Xe lamp (ORIEL Model 6269) replacing the He-Ne laser source.

Received 6 August 1984; revision received 25 September 1984.

* Author to whom correspondence should be addressed.

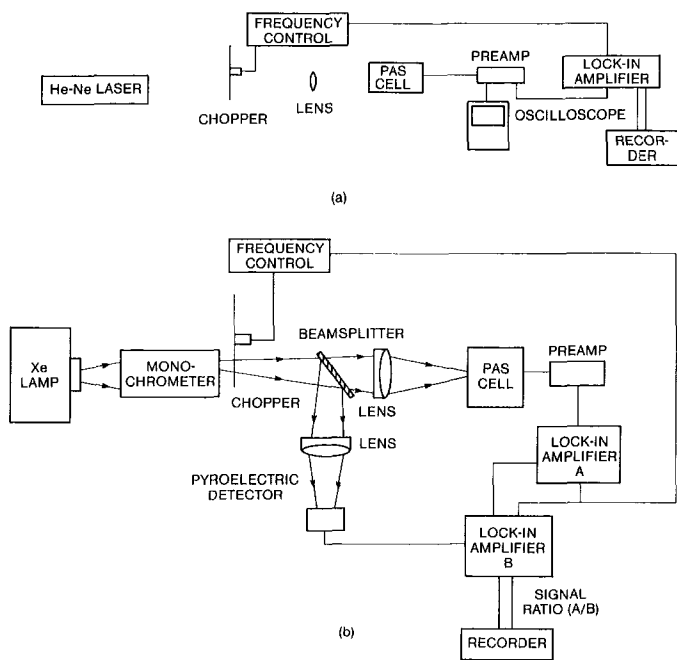


FIG. 1. Experimental apparatus: (a) geometry for PAS Frequency-Domain studies; (b) geometry for spectra acquisition in the UV-VIS region.

The specimens used in this work were two kinds: single-porosity and dual-porosity nickel electrodes. The single-porosity samples were pure nickel electrodes of known porosity used as references. The porosity distribution of these samples is shown in Fig. 2, which is the result of poisiometry measurements on a typical nickel electrode performed by Imperial Clevite, Cleveland, Ohio. No such measurements can be performed on dual-porosity nickel electrodes. The dual-porosity samples were obtained from Sherritt Gordon Mines Ltd./Sherritt Research Center, Fort Saskatchewan, Alberta, Canada. Table I describes the nominal specifications of these electrodes. All samples were cut in sizes of $\sim 9 \text{ mm} \times 6 \text{ mm}$ from large square specimens, the size being determined by the sample holder volume limitations. A sharp

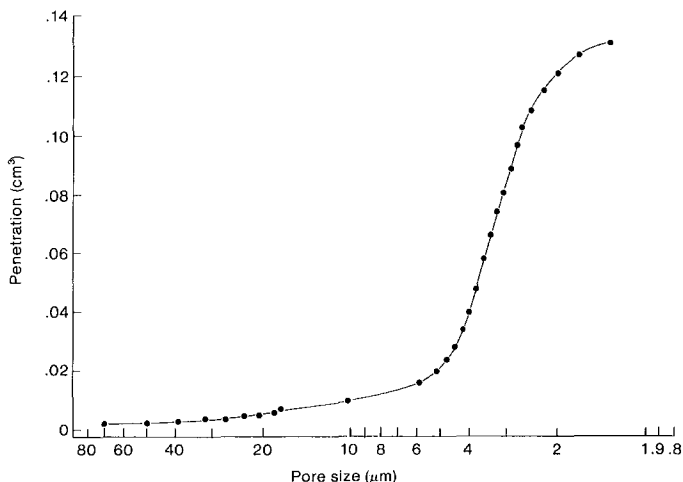


FIG. 2. Poisiometry results of pore size distribution in a pure nickel electrode. Mean pore size: $3.5 \mu\text{m}$ (Courtesy: Imperial Clevite, Cleveland, Ohio).

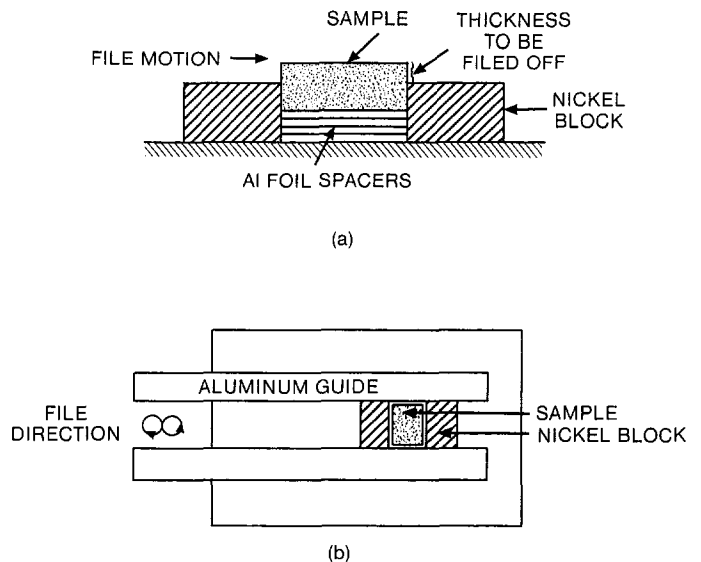


FIG. 3. Nickel electrode filing apparatus. (a) Cross-sectional side view. Al foil spacer thickness: $12.5 \mu\text{m}$. (b) Top view.

knife on a hard surface was used for the cutting, which minimized any deformation of the sample.

The experiments consisted of our filing known sample thicknesses off the surface of the dual-porosity electrodes and recording the frequency response of the PAS signal at 632.8 nm each time. Great care was taken in proper conditioning of the sample surface after each filing, to ensure consistent results. Figure 3 shows the home-made apparatus constructed for the purpose of uniform filing of known nickel thicknesses off the sample surface. A vernier caliper (micrometer) was used to measure sample thickness. The filing device allowed the accurate and reproducible removal of layers 0.0125 mm thick. Before the samples were put in the PAS cell, we found it necessary to clean all surfaces with compressed air. In this manner, very stable and reproducible signals were obtained, as the presence of any nickel-powder particulates on the surface tended to alter dramatically the magnitude of the photoacoustic signal. We found it necessary to remove thin nickel layers from the coarse-pore side of the electrodes only, as the dual-porosity samples exhibited a tendency to break up when the fine-pore layer was filed off and to subsequently crumble, due to the poor cohesion of the coarse layer.

In parallel with the PAS probe, image analysis was also used to characterize the cross-sectional porosity profile of the dual-porosity nickel samples. Image analysis of porous electrodes is a destructive technique, as it requires filling up of the pores with methylacrylic ester, which penetrates the sample via capillarity and so-

TABLE I. Specifications for dual-porosity pressed nickel electrodes.

Nominal specifications ^a	Fine-pore layer	Coarse-pore layer
Density (%)	41.2	22.8
Mean pore size (μm)	2.54	5.4
Thickness (mm)	0.56	1.04

^a Sherritt Gordon Mines Ltd., Fort Saskatchewan, Alberta, Canada; private communication.

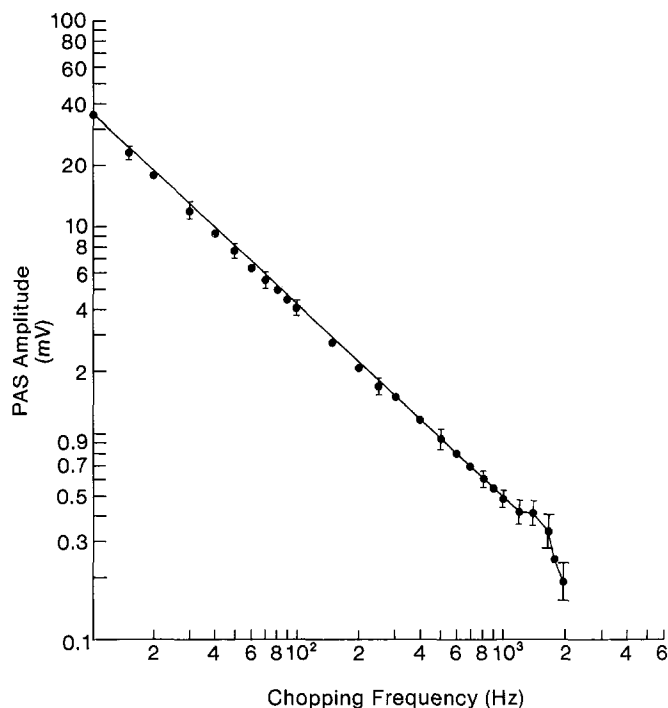


FIG. 4. PAS amplitude frequency response to He-Ne laser light from uniform, nominally uniporous nickel electrode. The actual pore size distribution is shown in Fig. 2.

lidifies upon oxygen starvation to form a solid interface strong enough to withstand cutting and polishing. Before a satisfactory television image of the cross-sectional surface could be obtained with a Digital Image Analyzer (Bausch and Lomb, OMNICON 3000), the samples had to be mounted in a solid matrix material, such as bakelite or resin. This was carried out in a mounting machine which provided the appropriate temperature and pressure for suitable mounting. The entombed samples were then polished until a very flat cross-sectional surface was exposed. To remove all scratches from the cross-sectional surface we had to use a fine-grade sandpaper whose grit size was less than the pore size in the samples.

RESULTS

Figure 4 shows the frequency response of the photoacoustic signal amplitude from a pure nickel, nominally single-porosity sample. The actual porosity distribution of the sample is shown in Fig. 2 and is centered around a pore size of $3.5 \mu\text{m}$. The frequency response of Fig. 4 exhibits an average slope of -0.9 ± 0.1 for frequencies below 1 kHz. The apparent anomaly at higher frequencies can be attributed to the relatively poor repeatability of the data above 1 kHz, despite a high signal-to-noise ratio. A mathematical correction scheme, used for all frequency plots in this work, was aimed at the elimination of the effects of Helmholtz resonances in the photoacoustic cell.^{3,4} For the EG&G PAS cell the peaks of the Helmholtz resonances were located at ~ 600 Hz, 1060 Hz, 1100 Hz, and 1200 Hz, as determined with the use of frequency plots of a black body (Xerox Toner), for which the PAS signal is optically saturated at all chopping frequencies used in this work. The correction of the

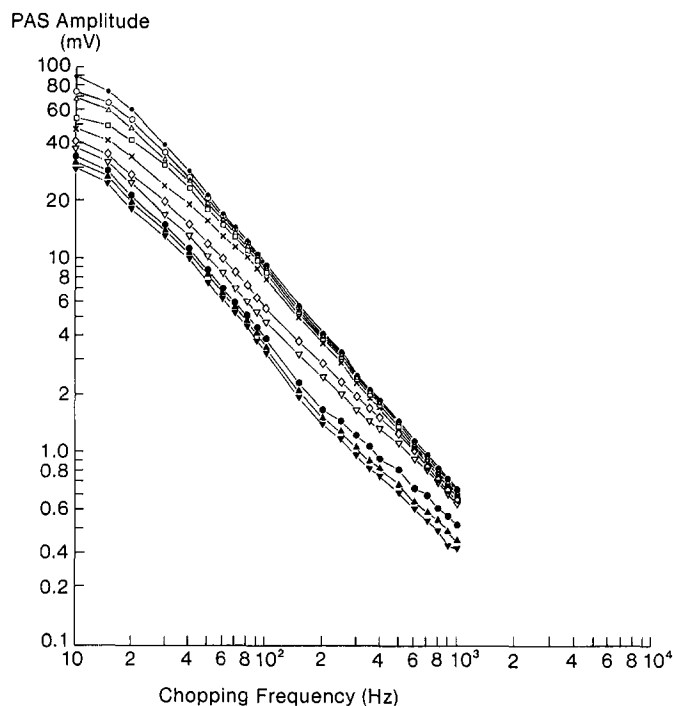


FIG. 5. PAS amplitude frequency response of a nominally biporous nickel electrode (Table I), with various thicknesses of the coarse-pore layer exposed to the He-Ne laser light. Coarse-pore layer thickness: (—●—●—) 1.04 mm; (—○—○—) 200 μm ; (—△—△—) 180 μm ; (—□—□—) 76 μm ; (—×—×—) 51 μm ; (—◇—◇—) 38 μm ; (—▽—▽—) 25 μm ; (—●—●—) 13 μm ; (—▲—▲—) 0.0 μm ; (—▼—▼—) response of fine-pore layer of the intact (i.e., before filing) biporous electrode.

pure nickel frequency plots eliminated the broad resonance peak centered at ~ 600 Hz. It proved inadequate, however, to eliminate the resonant peaks above 1 kHz, due to the magnitude of the uncertainty involved with the observed large signal variations within relatively narrow frequency span. Therefore, we decided to reject data at frequencies higher than 1 kHz from all subsequent experiments.

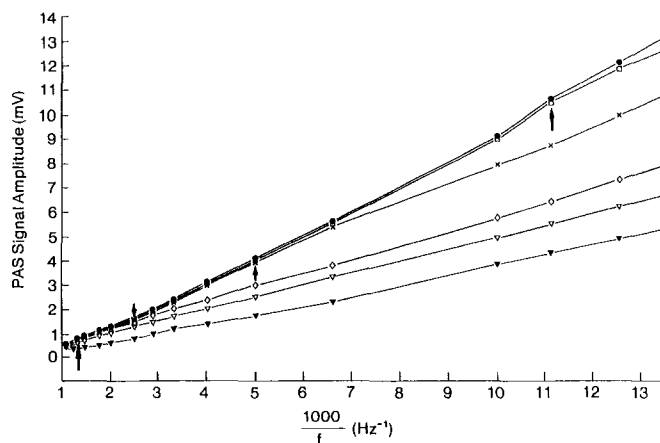


FIG. 6. PAS frequency response amplitude of the sample in Fig. 5, plotted against inverse chopping frequency. Curves correspond to the following coarse-pore layer thicknesses: (—●—●—) 1.04 mm; (—□—□—) 76 μm ; (—×—×—) 51 μm ; (—◇—◇—) 38 μm ; (—▽—▽—) 25 μm ; (—▼—▼—) 0.0 μm . The arrows indicate the average frequency f_0 at which the onset of the separation between two consecutive curves occurs.

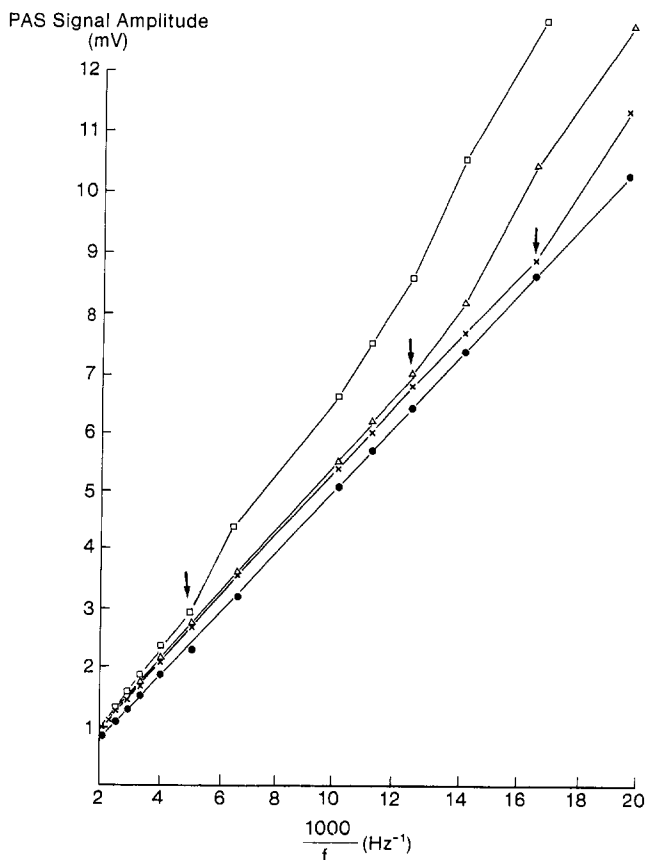


FIG. 7. PAS amplitude vs. inverse frequency of a nominally biporous nickel electrode (Table I), with various thicknesses of the fine-pore layer exposed to the He-Ne laser light. Fine-pore layer thickness: (—●—●—) 560 μm ; (—×—×—) 152 μm ; (—△—△—) 127 μm ; (—□—□—) 76 μm . The arrows indicate the average frequency f_0 at which the onset of the separation between two consecutive curves occurs.

Figure 5 is a log-log plot of the photoacoustic amplitude vs. chopping frequency from the nominally dual-porosity electrode samples (Table I), corrected for the Helmholtz resonance effects. The curve with highest amplitude corresponds to PAS signals from an intact electrode, whose coarse-pore surface was exposed to the He-Ne laser probe beam. The intermediate amplitude curves correspond to the same electrode with the coarse-pore surface exposed to the light and various thicknesses of the coarse-pore layer filed off. The PAS amplitude frequency response is no longer a linearly decreasing function of frequency, as was the case in Fig. 4. In the limit of zero-thickness coarse-pore layer, the coarse-pore and fine-pore curves essentially coincide, while for finite coarse-pore layer thicknesses each curve separates off from the immediately overlying curve below some characteristic frequency. These characteristic frequencies f_0 increase as the coarse-pore layer thicknesses decrease.

Figure 6 is an alternative presentation of some of the dual-porosity data of Fig. 5. The plots vs. f^{-1} exhibit essentially linear regions separated by transitional regions which occur at different frequencies, depending on the thickness of the coarse-pore layer. The arrows have been placed at the chopping frequency which represents the onset of the separation between two curves. Yun and Seo⁵ have reported similar behavior of the PAS signal

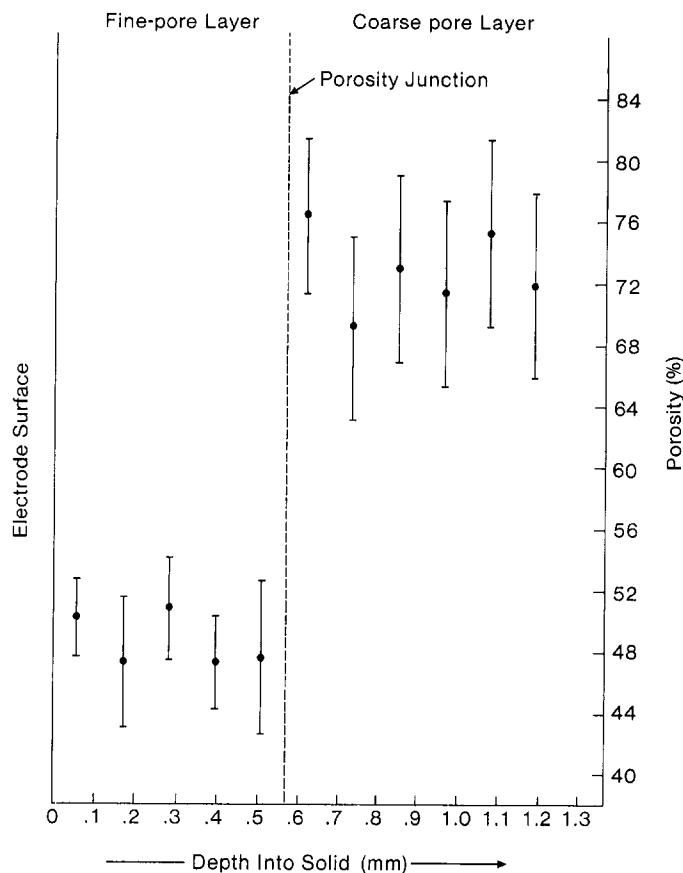


FIG. 8. Biporous nickel electrode porosity profile from Image Analysis. Statistical averages of four scans on the electrode cross-section.

from a Cu/adhesive/Cu multilayer structure. These authors have associated the transitional regions of the PAS amplitude vs. f^{-1} plots with characteristic chopping frequencies f_0 , for which a material layer of a given thickness passes from the thermally thin limit (i.e., $\mu_j > L_j$) to the thermally thick limit (i.e., $\mu_j < L_j$). At f_0

$$\mu_j(f_0) = (\alpha_j/\pi f_0)^{1/2} = L_j, \quad (1)$$

where $\mu_j(f_0)$ is the thermal diffusion length of the j th layer at f_0 , α_j is the thermal diffusivity of the j th layer, and L_j is its thickness. Equation 1 can be used to determine the thermal diffusivity of a material, from its (known) thickness L_j and the transitional frequency of the PAS amplitude vs. f^{-1} plot. The procedure outlined for various coarse-pore layer thicknesses above was also repeated for a few values of the fine-pore layer thickness of a sample from the same dual porosity specimen. The results are shown in Fig. 7, with the minimum fine-pore layer thickness determined by the ability of the underlying coarse-pore layer to support that layer without breaking up or crumbling. The calculated values of the thermal diffusivity of each of the two layers from Figs. 6 and 7 and Eq. 1 are shown in Table II. For parameter calculation, allowance was made for the uncertainty in the actual value of the transitional frequency, by the acceptance of frequency values within a transition frequency band characterized by the steep slope regions of Figs. 6 and 7. The average values for the coarse-pore and fine-pore layer thermal diffusivities are seen to be

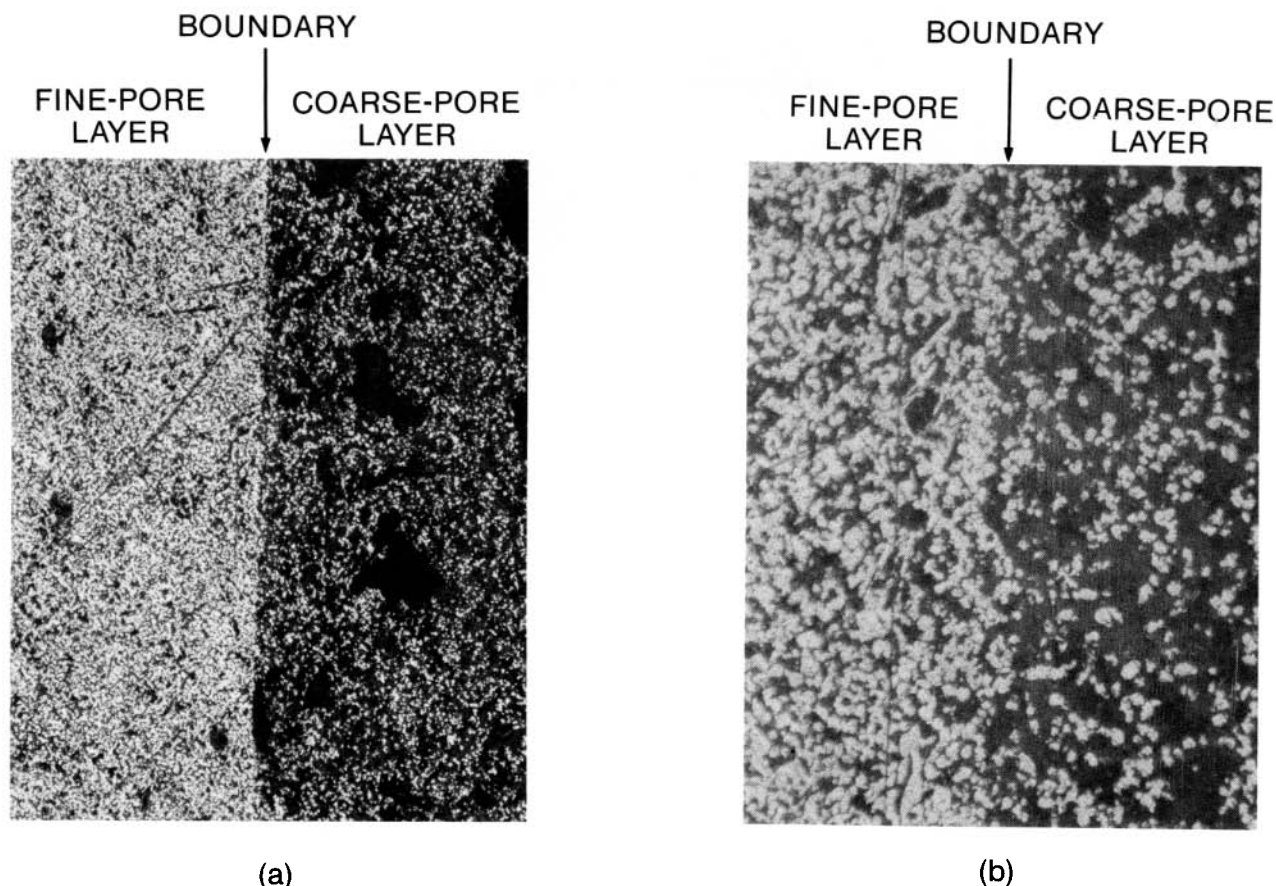


FIG. 9. Photographs of the porosity junction in the bipolar electrode. (a) Magnification 100 \times . Randomly distributed large voids are visible in the coarse-pore layer bulk. (b) Magnification 400 \times .

much lower than that of metallic nickel (0.21 cm²/s at 320°K).⁶ This result is consistent with observations by Bertrand *et al.*,^{7,8} who calculated the values of the thermal diffusion lengths of powdered materials (chrysotile asbestos, alumina) and compared them to those of continuous phases (e.g., solid alumina). These authors consistently reported lower values for thermal diffusion lengths (and, therefore, thermal diffusivities) for the powdered samples.

Figure 8 is a porosity depth profile of the dual-porosity sample before any layer removal, calculated by the Digital Image Analyzer. The large error bars are the re-

sult of fourfold averaging and are partly due to inherent systematic errors of calculations made by this device, namely (1) the nonuniform illumination over the field, and (2) the operator's subjective decision of inclusion of borderline gray regions into the dark (indicating "porous") area count, or into the bright (indicating "solid") area count. Table III shows that the digitally calculated average porosities of the two layers are essentially in agreement with the nominal values calculated from Table I. Both the image analysis data, Fig. 8, and optical microscope photographs, Fig. 9, show the presence of an abrupt porosity junction in the electrode material. Nevertheless, it is interesting to note the existence of a few large voids, especially within the bulk of the coarse-pore layer, Fig. 9. The origin of these voids is unknown at present.

Figure 10 shows the PAS spectrum of a single-porosity nickel electrode obtained with the experimental configuration of Fig. 1b. The spectrum is normalized by the

TABLE II. Thermal diffusivity values for coarse-pore and fine-pore layers of dual-porosity pressed nickel electrode, calculated with the use of Eq. 1 and Figs. 6 and 7.

Layer	Thickness (mm)	Transition frequency range (Hz)	Calculated thermal diffusivity $\times 10^2$ (cm ² /s)	Average thermal diffusivity $\times 10^2$ (cm ² /s)
Coarse	0.076	80-90	1.4-1.6	1.77 \pm 0.8
	0.051	200-250	1.6-2.0	
	0.038	400-500	1.8-2.2	
	0.025	800-900	1.6-1.8	
Fine	0.076	200-300	5.5-3.6	4.9 \pm 2.0
	0.127	100-150	7.5-5.1	
	0.152	50-60	4.4-3.7	

TABLE III. Computer statistical calculations of average porosities of bipolar electrode with the use of Image Analysis.

Layer	Average porosity (image analysis)	Nominal porosity (from Table I)
Coarse	73 \pm 8%	77.2%
Fine	49 \pm 4%	58.8%

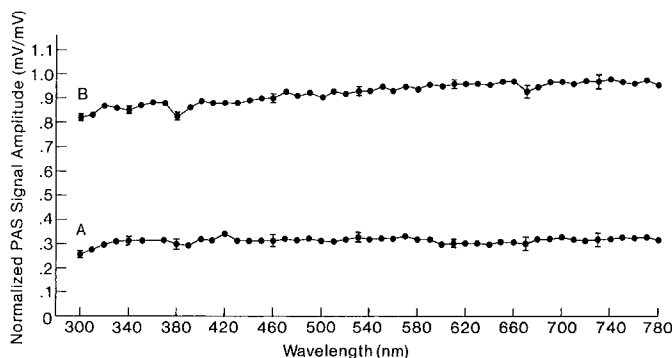


FIG. 10. Photoacoustic spectra of a uniporous nickel electrode (A) and INCO nickel powder type 255 (B). Resolution: 8 nm; lock-in time constant: 1 s.

Xenon lamp spectrum, which was taken with the use of a black absorber (Xerox Toner). In the same figure, the spectrum of nickel powder (INCO® powder type 255)⁹ is shown for comparison. Both spectra exhibit photoacoustic saturation¹⁰ throughout the 300–780 nm wavelength region, with a slight monotonic increase of the nickel powder signal toward the longer wavelengths. These results are in contrast with optical spectra of solid metallic Ni reported by Lenham.¹¹ The values for the optical absorption coefficient for Ni between 300 nm and 1 μm shown in Ref. 11 lie between 15 cm^{-1} and 30 cm^{-1} . This would suggest that nickel powders and pressed electrodes may be expected to be photoacoustically far from saturation, if light absorption mechanisms are not fundamentally different between the solid and the powdered metal. No explanation of the discrepancy is firmly established at present; however, it is plausible that the nominally pure nickel samples used in this work may have been contaminated during manufacture with some highly absorbing species, such as carbon particulates. This would be consistent with the carbonyl-gas refining process used for the treatment of INCO nickel powders, which incorporates 0.2% weight of carbon to the powder.¹²

COMPARISON WITH THEORY AND DISCUSSION

The frequency response of the uniporous nickel electrode, Fig. 4, exhibits a $\omega^{-0.9 \pm 0.1}$ dependence. The phase channel of the photoacoustic signal has also been considered as an alternative depth-profiling information source; however, reproducibility proved to be much poorer than that of the amplitude channel. The reason(s) for the large uncertainties in the value of PAS phase as a function of chopping frequency are not clear at present. A possible explanation may lie in the fact that the phase is more sensitive to local thermal property variations than the amplitude at a given depth in a material, determined by the thermal diffusion length.¹³ The existence of large voids within the bulk of the nickel electrodes may have introduced thermal inhomogeneities locally, which could be responsible for the large phase variations from one site to another at the same chopping frequency.

The amplitude frequency dependence of the uniporous nickel electrode, Fig. 4, along with the spectrally

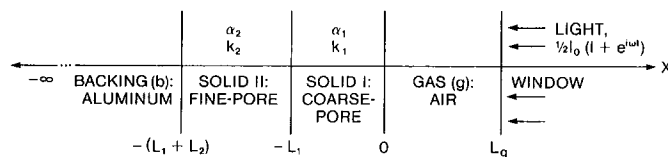


FIG. 11. Geometry for a double-layer PAS system.

saturated curve A in Fig. 10, is consistent with the optically opaque, thermally thick limit of the one-dimensional Rosencwaig-Gersho theory,¹⁰ case 5.2(b), which was developed for a continuous, absorbing solid. Therefore, it can be argued that in the frequency range of interest the porous, pressed nickel electrode behaves photoacoustically like an optically opaque and thermally thick continuous solid. This behavior simplifies greatly the analytical treatment of such an electrode, with respect to calculations of its effective thermal properties (i.e., diffusivity and conductivity) from the photoacoustic data.

The frequency-domain photoacoustic data from the dual-porosity nickel electrodes, Fig. 5, were compared with predictions of a one-dimensional double layer PAS theoretical model proposed for continuous solids by Mandelis *et al.*¹⁴ The general two-layer model of Ref. 14 was taken in the limit of optically opaque solids, in agreement with the photoacoustically saturated curve A of Fig. 10. For excitation at 632.8 nm the optically opaque PAS signal is given by:

$$P(\omega) = (\gamma P_0 / \sqrt{2} L_g T_0 a_g) T_s(x=0, \omega) \quad (2)$$

where ω is the angular chopping frequency, and the various quantities in parentheses were defined elsewhere.^{10,14} $T_s(x=0, \omega)$ is the upper layer temperature at the gas (air)-solid interface, Fig. 11. For optically opaque solid layers 1 and 2, the interface temperature is:¹⁴

$$T_s(0, \omega) = \left(\frac{I_0}{2k_1\sigma_1} \right) [(b_1 + 1)(b_2 + 1)\exp(\sigma_1 L_1 + \sigma_2 L_2) + (b_1 - 1)(b_2 - 1)\exp(\sigma_1 L_1 - \sigma_2 L_2) - (b_1 + 1)(b_2 - 1)\exp(-\sigma_1 L_1 - \sigma_2 L_2) - (b_1 - 1)(b_2 + 1)\exp(-\sigma_1 L_1 + \sigma_2 L_2)] / [(b_1 + 1)(b_2 + 1)\exp(\sigma_1 L_1 + \sigma_2 L_2) + (b_1 - 1)(b_2 + 1)\exp(-\sigma_1 L_1 + \sigma_2 L_2) + (b_1 + 1)(b_2 - 1)\exp(-\sigma_1 L_1 - \sigma_2 L_2) + (b_1 - 1)(b_2 - 1)\exp(\sigma_1 L_1 - \sigma_2 L_2)] \quad (3)$$

where I_0 is the incident light intensity (W/cm^2), assumed spatially uniform, L_1 and L_2 are the layer thicknesses, and

$$\sigma_j \equiv (1 + i)(\omega/2\alpha_j)^{1/2}; \quad j = 1, 2 \quad (4)$$

$$b_1 \equiv k_2 \sqrt{\alpha_1} / k_1 \sqrt{\alpha_2} \quad (5)$$

and

$$b^2 \equiv k_b \sqrt{\alpha_2} / k_2 \sqrt{\alpha_b}; \quad (6)$$

k_j is the thermal conductivity of material (j); $j = 1, 2, b$. The backing material (b) for the experiments in this work was aluminum, whose thermal properties are:¹⁵ $\alpha_{Al} = 0.82 \text{ cm}^2/\text{s}$, $k_{Al} = 2.01 \text{ W}/\text{cm} \text{ }^\circ\text{K}$. Solid layer 1 was identified with the coarse-pore layer, and solid layer 2 with the fine-pore layer in the $\ln|P(\omega)|$ vs. $\ln f$ plots of

Fig. 12. In that figure, only four curves from Fig. 5 were considered, so clustering of data in one figure could be avoided. Equation 2 was fitted to one of the curves (curve D), with the use of α_1 , α_2 , b_1 , and b_2 as variables for the best fit. This occurred for the set of values:

$$\alpha_1 \equiv \alpha_c = 2.8 \times 10^{-2} \text{ cm}^2/\text{s} \quad (7a)$$

$$\alpha_2 \equiv \alpha_f = 5 \times 10^{-2} \text{ cm}^2/\text{s} \quad (7b)$$

$$b_1 = 2.4 \quad (7c)$$

$$b_2 = 10. \quad (7d)$$

The above values for α_1 and α_2 are consistent with the averages of Table II, with α_1 being somewhat higher than the calculated average. Use of the values 7a–7d in Eqs. 5 and 6 gives the optimal values for the thermal conductivities, based on the fit to Fig. 12, curve D ($L_1 \equiv L_c = 13 \mu\text{m}$)

$$k_1 \equiv k_c = 1.55 \times 10^{-2} \text{ W/cm }^\circ\text{K} \quad (8a)$$

and

$$k_2 \equiv k_f = 4.96 \times 10^{-2} \text{ W/cm }^\circ\text{K}. \quad (8b)$$

The values for α_1 , α_2 , k_1 , k_2 , b_1 , b_2 from Eqs. 7 and 8 were further used to fit curves A–C in Fig. 12. It can be seen that the fit to curves A and D is very good for frequencies higher than ~ 20 Hz, while the fits to curves B and C show some departure from the data slopes. The low-frequency departures of all data curves below the theoretical lines of Fig. 12 may be due to lateral dissipation of heat around the laser beam center, which would introduce three-dimensional effects not accountable by the simple one-dimensional theory.¹⁶ The discrepancy observed at higher frequencies between experiment and the theoretical curves B and C cannot be explained in simple terms; it is very likely due to the porous nature of the samples. From a different point of view, the close correspondence between the experimental and the theoretical curves of Fig. 12 suggests that the complex-structured, discontinuous nickel electrodes with dual-porosity depth profiles may be approximately treated as double-layer continuous solids. The advantages of this approach are (1) the relative simplicity of the calculations involved in interpreting the PAS signal, when compared to complicated, albeit more realistic, theoretical models^{3,17–19}; and (2) the ability to estimate values for the effective thermal properties (diffusivity and conductivity) of each porous layer L_j , provided its thickness is known. This type of calculation is very difficult to perform with more realistic (i.e., more complex) mathematical models, and essentially impossible to obtain nondestructively with other techniques. A second possible source of the discrepancy between theory and some experimental data in Fig. 12 is the random presence of large voids on the coarse-pore side of the porosity junction, as shown in Fig. 9. These voids can be expected to act as regions of high thermal resistance, which would tend to render the simple, homogeneous, one-dimensional model of Eqs. 2 and 3 locally invalid, at thermal diffusion lengths and/or laser beam diameters smaller than, or on the order of, the mean void diameter.

The estimated values 8a and 8b for the thermal conductivities of the coarse- and fine-pore layers, respectively, indicate a trend for increased thermal conductivity with decreasing porosity. This observation is

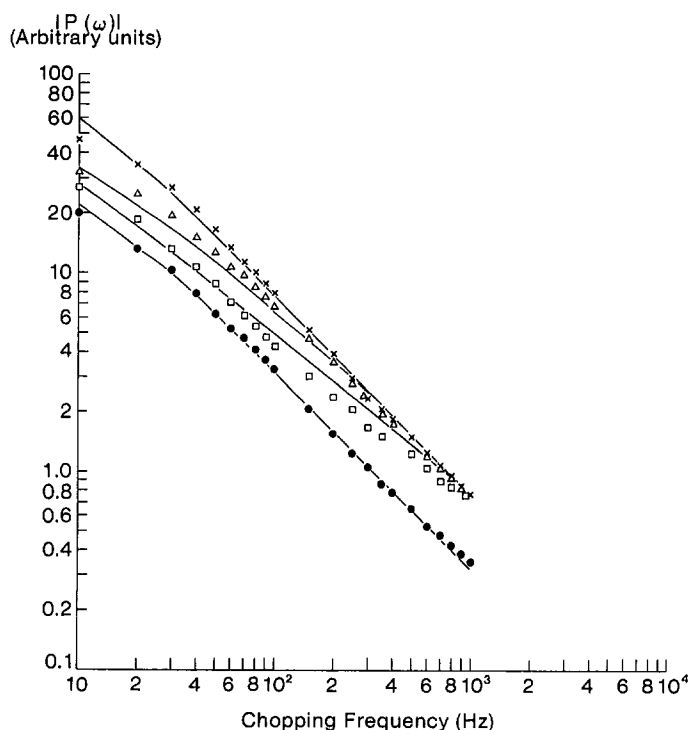


FIG. 12. Least-squares fit of PAS amplitude frequency response, Fig. 5, to the model of Eqs. 2 and 3. Coarse-pore layer thickness L_1 : A, (\times) 200 μm ; B, (\triangle) 76 μm ; C, (\square) 25 μm ; D, (\bullet) 13 μm . Fine-pore layer thickness $L_2 = 0.56$ mm.

consistent with similar trends reported for MgO , Al_2O_3 , and ZrO_2 powders of variable (controlled) pore sizes.²⁰ It should be mentioned that the thermal conduction experiments in Ref. 20 required complicated apparatus and accurate calibrations in well-controlled thermal environments, as opposed to the relative ease of photoacoustic data acquisition with no need for calibrations, and no worse uncertainty in the thermal conductivity calculations than that in Ref. 20.

CONCLUSIONS

In this study, Frequency-Domain PAS was used as a depth-profiling analytical tool to give reasonable estimates for the values of thermal diffusivities and conductivities of powdered, pressed, optically opaque nickel electrodes with a step-functional porosity profile. For these calculations accurate knowledge of the depth of the porosity junction was necessary; however, the estimated thermal property values could be used, conversely, to calculate porosity junction depths of other dual-porosity nickel electrodes from the PAS amplitude vs. chopping frequency plots. A one-dimensional mathematical model, principally valid for a double layer of continuous solids, was shown to be a reasonable fit to the experimental data, which suggests an approximately continuous solid behavior of the porous pressed electrodes, thus simplifying enormously the task of interpretation. Similarly, the PAS data from uniporous electrodes exhibited behavior expected of a uniform, continuous solid in conformity with the Rosencwaig-Gersho model. This analysis demonstrates the potential

use of PAS as a nondestructive technique to monitor porosity profiles via thermal conductivity and diffusivity calculations for the individual porous layers of fuel cell electrodes *in situ* during operation for long-term testing. The ability of Frequency-Domain PAS to calculate effective values for porous material thermal properties can be utilized in fuel cell electrode degradation studies, where significant variations of the thermal properties of individual porous layers are expected, subsequent to electrolyte and/or gas penetration into the electrode bulk.

ACKNOWLEDGMENT

The authors wish to express their appreciation to the Natural Science and Engineering Research Council of Canada (NSERC) for financial support of this work.

1. B. J. Crowe, *Fuel Cells; a Survey* (Technology Utilization Office Publication, National Aeronautics and Space Administration, Washington DC, 1973; NASA SP-5115).
2. M. H. Miles, G. Kissel, P. W. T. Lu, and S. Srinivasan, *J. Electrochem. Soc.* **123**, 332 (1976).
3. N. C. Fernelius, *Appl. Opt.* **18**, 1784 (1979).
4. R. S. Quimby, P. M. Selzer, and W. M. Yen, *Appl. Opt.* **16**, 2630 (1977).

5. S. I. Yun and H. J. Seo, Technical Digest, 3rd International Topical Meeting on Photoacoustic and Photothermal Spectroscopy, April 5-8, 1983, Paris, France, paper 6.2/2.
6. Y. S. Touloukian, *Thermal Diffusivity* (IFI/Plenum, New York, 1973).
7. L. Bertrand, J. P. Monchalain, and F. Lepoutre, *Appl. Opt.* **21**, 248 (1982).
8. J. P. Monchalain, L. Bertrand, and F. Lepoutre, "Photoacoustic Spectroscopy of Thick Powdered or Porous Samples at Low Frequency," unpublished.
9. N. J. Williams, D. J. Burr, and P. J. Bridges, *Powder Metallurgy* **15**, 42 (1972).
10. A. Rosencwaig and A. Gersho, *J. Appl. Phys.* **47**, 64 (1976).
11. A. P. Lenham, *J. Opt. Soc. Am.* **57**, 473 (1967).
12. INCO Nickel Powder Type 255, INCO Metals Co., Technical Specification 5M 8-75, A-1185 A, Toronto, Ontario, Canada.
13. A. Rosencwaig and G. Busse, *Appl. Phys. Lett.* **36**, 725 (1980).
14. A. Mandelis, Y. C. Teng, and B. S. H. Royce, *J. Appl. Phys.* **50**, 7138 (1979).
15. A. Rosencwaig, *Photoacoustics and Photoacoustic Spectroscopy* (J. Wiley, New York, 1980), p. 96.
16. R. S. Quimby and W. M. Yen, *Appl. Phys. Lett.* **35**, 43 (1979).
17. P. Helander, I. Lundström, and D. McQueen, *J. Appl. Phys.* **51**, 3841 (1980).
18. L. W. Burggraf and D. E. Leyden, *Anal. Chem.* **53**, 759 (1981).
19. P. Helander, Ph.D. Thesis, Linköping Inst. of Technology, Linköping, Sweden (1983).
20. H. W. Godbee and W. T. Ziegler, *J. Appl. Phys.* **37**, 40 (1966); and *J. Appl. Phys.* **37**, 56 (1966).

Curve Fitting of Heterodyne Data

B. R. REDDY

Department of Physics, Memorial University of Newfoundland, St. John's, NFLD A1B 3X7, Canada

The least-squares curve fitting procedure of experimental data is described for heterodyne detection. Two independent methods, the Maximum Likelihood method of Fisher and SIMPLEX, have been tried. The relative merits and limitations are discussed in detail.

Index Headings: Heterodyne spectroscopy; Curve fitting.

INTRODUCTION

Phase-sensitive heterodyne detection is one of the most sensitive spectroscopic techniques used in the measurement of weak signals with high signal-to-noise ratio. Both absorption and dispersion associated with the spectral feature of interest can be selectively measured by the monitoring of the phase^{1,2} and is possible only for a perfect setting of the phase adjuster. Phase-adjuster setting is not a simple task and depends on the response of the device used for this purpose. But for any intermediate settings of the phase adjuster (which is quite likely), the output of the double balanced mixer (DBM) produces mixed lineshapes and complicates the data analysis. A sample spectrum is shown in Fig. 1, where the peaks are a convolution of dispersion (major component) and absorption (minor component). In order for one to obtain best estimates of the hyperfine interaction parameters,

voluminous data of this type must be analyzed. An accurate estimate of linewidth is more important if one is to make any meaningful comparison of line broadening mechanisms with the measurements. In cases where it is neither simple nor easy to correct the experiment, theory should account for the experimental difficulties. This latter aspect is discussed in this paper. The theory used should be more general in order to describe the experimental data of any form, absorption/dispersion/convolution (mixed line shape). We could successfully describe heterodyne data using

$$y = Z_1 A \cos \Theta \frac{x - \mu}{\sigma^2} \exp\left(\frac{-(x - \mu)^2}{2\sigma^2}\right) + Z_2 A \sin \Theta \exp\left[\frac{-(x - \mu)^2}{2\sigma^2}\right] \quad (1)$$

for Gaussian lineshapes, and

$$y = \frac{Z_1 A \cos \Theta (x - \mu) \Gamma}{[(x - \mu)^2 + (\Gamma/2)^2]^2} + \frac{Z_2 A \sin \Theta (\Gamma/2)}{[(x - \mu)^2 + (\Gamma/2)^2]} \quad (2)$$

for Lorentzian lineshapes where μ is the peak frequency,

Received 26 October 1984.